A Method for Estimating Object Detection Probability, Lateral Resolution, and Errors in 3-D LiDARs

Stefano Cattini, *Member, IEEE*, Davide Cassanelli, *Graduate Student Member, IEEE*, Luca Ferrari, and Luigi Rovati, *Member, IEEE*

***Abstract*— The 3-D light detection and rangings (LiDARs) are nowadays used for many applications, the success of which certainly depends on the processing of the LiDAR output—the point cloud (PC)—but it also inexorably depends on the quality of the PC data. In this study, we propose an experimental method aimed at allowing estimating the errors and deformations that will statistically affect the LiDAR output—the PC. Taking advantage of the fact that LiDARs sample the surrounding space by observing it along divergent lines, hereinafter referred to as rays, this study proposes a simple method based on the experimental determination of the ray detection probability—the probability that a single ray detects the hit object, or a fraction of it, by adding a point in the PC. All other probabilities of interest are derived from such a probability. The proposed method also allows highlighting unexpected errors, such as crosstalk. As will be shown by the examples given, due to crosstalk, small objects may be deformed and enlarged on a significantly greater number of points in the PC. Likewise, objects angularly separated by an angle greater than the angular resolution declared by the manufacturer may unexpectedly result in a continuum of points. Such errors may compromise the ability to perform very important tasks, such as detection, classification, and tracking of dynamic and static objects, as well as the partition of the scene into drivable and non-drivable regions and the path planning around generic obstacles in 3-D space.**

***Index Terms*— Autonomous driving, classification, detection, lateral resolution, light detection and ranging (LiDAR), object detection probability, scene partition.**

I. Introduction

DRIVEN by the objective of autonomous driving, the automotive sector is pouring huge investments into the development of increasingly performing, reliable, and economical 3-D light detection and ranging (LiDAR) systems. Such has resulted in a renewed research interest that has led to several studies on the design, calibration, characterization, and benchmarking of 3-D LiDAR systems and subsystems, e.g., [1], [2], [3], [4], [5], [6], [7], [8], [9], [10], [11], [12], [13].

Manuscript received 4 March 2023; revised 6 May 2023; accepted 24 June 2023. Date of publication 24 July 2023; date of current version 9 August 2023. The Associate Editor coordinating the review process was Dr. Yang Bai. *(Corresponding author: Stefano Cattini.)*

Stefano Cattini and Luigi Rovati are with the Department of Engineering "Enzo Ferrari" and the Interdepartmental Centre Intermech MO.RE., University of Modena and Reggio Emilia, 41125 Modena, Italy (e-mail: stefano.cattini@unimore.it).

Davide Cassanelli is with the Department of Engineering "Enzo Ferrari," University of Modena and Reggio Emilia, 41125 Modena, Italy.

Luca Ferrari is with CNH Industrial Italia SpA, 41122 Modena, Italy.

Digital Object Identifier 10.1109/TIM.2023.3298392

Basically, for all applications and especially for 3-D objects perception (detection, classification, and tracking of dynamic and static objects) and scene segmentation (e.g., partition the scene into drivable and non-drivable regions), the objects detection probabilities, as well as the deformations introduced in the objects representation in the point cloud (PC) and the lateral resolution, represent aspects of considerable importance. However, such information is not provided by LiDARs manufacturers. Actually, manufacturers usually provide the angular sampling period, often indicating this parameter with the improper term "angular resolution." As will be discussed in more detail in the following sections and shown by the reported experimental results, using this value as the lateral resolution can lead to significant errors.

For the lateral resolution analysis, two methods have essentially been proposed [11]: one based on the measurement of the size of the LiDAR beams at different axial distances [5], and the other based on the acquisition of the image of cubic targets and on the subsequent analysis of blurring in the targets representation in PC [1], [11].

Since LiDARs sample the surrounding space by observing it along divergent lines, hereinafter referred to as rays, in this study, we propose a measurement method that, based on experimental measurements, is capable of estimating the probability that a specific ray gives rise to a point in the PC. From the knowledge of this probability, it is possible to estimate parameters, such as, for example, the minimum cross section that an object must have for its detection probability to be higher than a certain threshold value, as well as the minimum angular distance that must separate two objects, so that the probability that they are distinguishable in the PC is higher than a certain value. Furthermore, as will be described later on, the proposed method also makes it possible to highlight and quantify all kinds of errors that can afflict the PC, some of which, such as crosstalk, are potentially unexpected. To the best of our knowledge, studies aimed at experimentally estimating such quantities have not been proposed in the literature to date.

In the following, Section II briefly recalls the operating principle of 3-D LiDARs and introduces the probabilities and errors that the proposed method is intended to analyze. Section III recalls the quantities that contribute to determining the intensity of the signal received by the LiDAR, and Section IV describes in detail the proposed method, describing the required experimental characterizations, the

proposed statistical analysis, and the intrinsic limits of applicability. To provide an idea of the information that can be obtained, Section V and the Appendix report some example results obtained by investigating the LiDAR model MRS 6000 by SICK. Finally, the discussion and conclusions are reported in Sections VI and VII, respectively.

II. Statement of the Problem

The 3-D LiDARs analyze the surrounding environment by analyzing the echoes that the emitted beams generate after specular and/or diffuse reflection. Scanning LiDARs steer one or more collimated laser beams to sequentially scan the surroundings. The coordinates of the points of the PC are then determined by the spherical coordinates (azimuth, θ, and elevation, φ) defined by the emitted pulses [6]. Similarly, in flash LiDARs, the points of the PC are determined by the "line of sight" of the detectors that compose the photodetector array [6]. Hence, regardless of the technology, all 3-D LiDARs acquire the PC sampling the surrounding in spherical coordinates [6]

$$p = (r, \theta, \varphi). \tag{1}$$

The radius, r, of each point of the PC is usually determined from a time-of-flight (ToF) measurement. Such a ToF measurement can be "direct"—pulse telemeters—or "indirect"—sine-wave telemeters [14]. In pulsed—direct ToF—LiDARs, currently, the most used technology for automotive applications [15], the set of allowed radii is primarily determined by the time-to-digital converter, which determines the axial quantization step Δr [6].

Except for some special cases mainly related to the research field, e.g., [7], [9], basically for all LiDARs currently on the market, the spatial sampling takes place along predefined and constant rays, therefore, the set of "admitted values," the domain, if finite—only a restricted number of elevation angles, φ, azimuth angles, θ, and radii, r, is allowed. The advent of solid-state LiDARs and the consequent absence of moving parts suggest that this will likely continue to represent the operating condition for most commercial LiDAR systems.

The rest of the discussion will refer to LiDARs for which sampling occurs along a set of predefined and constant rays.

The nominal "vertical" angular sampling period $\Delta\varphi$—the difference in elevation angle between adjacent points along the "vertical" direction—is generally improperly indicated by manufacturers with the term "vertical angular resolution," whereas the difference in azimuth angle between adjacent points along the "horizontal" direction, the nominal "horizontal" angular sampling period $\Delta\theta$, is generally improperly referred to as the "horizontal angular resolution." The angular sampling periods $\Delta\varphi$ and $\Delta\theta$ are usually declared by the manufacturer (generally under the improper term resolution) and, if not, can be easily estimated by analyzing the PC in spherical coordinates [6].

Regardless of where the object that created the received echo is, PC points can only be found along a finite set of diverging straight lines—the rays—angularly spaced by the azimuth ($\Delta\theta$) and elevation ($\Delta\varphi$) angular periods. Every single point is, thus, located along the ray defined by the nominal optical axis of the beam that generated such an echo (scanning LiDARs), that is, along the line of sight of the pixel that received the echo (flash LiDARs) and, at a distance, defined by the Δr multiple that best approximates the real object distance. Fig. 1 shows an out-of-scale 2-D representation of how 3-D LiDARs approximate the surroundings due to quantization.

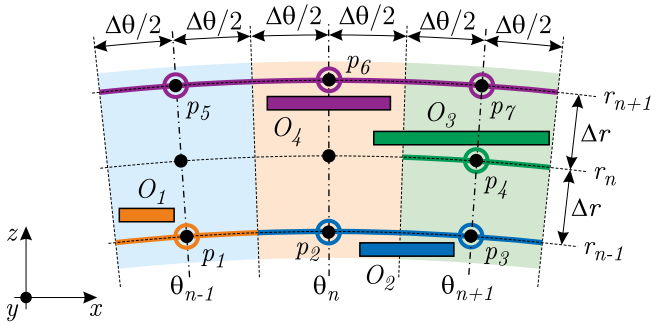

Fig. 1. Schematic 2-D representation of the quantization and errors introduced by 3-D LiDARs. The figure shows the "top view" of how a single LiDAR channel—fixed elevation angle φ_m—analyzes the environment. The three vertical dashed-dotted lines represent the "rays," that is, the optical axes of the beams sequentially emitted by the LiDAR (scanning LiDARs) or the lines of sight of the receivers of the same channel (flash LiDARs). Each of them is spaced $\Delta\theta$ to the adjacent. The dashed "horizontal" semicircles represent the axial quantization. Each of them constitutes a bin, and its radius differs Δr from the adjacent. The dots (•), thus, represent the only values that the points in the PC can assume. The circles (o) represent the points of the PC—the result of the sampling of the environment by the LiDAR. The bold solid horizontal semicircles show how the specific object is reconstructed in the PC. As shown, the object O_1 is approximated with point p_1 at the coordinates $(r_{n-1}, \theta_{n-1}, \varphi_m)$. Assuming that a point p in the PC represents an object or a portion of an object having the center in p, "vertical" angular extension $\pm\Delta\varphi/2$, and "horizontal" angular extension $\pm\Delta\theta/2$, the object O_1 is, thus, both enlarged (type-1 error, enlargement) and shifted, since its center does not coincide with p_1 (type-3 error, shift). The object O_2 affects two rays, and since it is reconstructed in the PC with points p_2 and p_3, it is affected by both enlargement and shift errors, since the $\overline{p_2 p_3}$ center does not coincide with the O_2 center. The O_3 object represents the opposite case with respect to the O_2 object since, although it affects two adjacent rays, it is represented by the LiDAR with only the p_4 point (type-2 error, shrinkage). In addition to being restricted, the O_3 object is also shifted (type-3 error, shift). The O_4 object is represented in the PC by points p_5, p_6, and p_7. Such an error (type-4 error, crosstalk) will be described in more detail in the next sections. If the object involves several adjacent beams, it is also possible that some of the points inside the object are missing in the PC. That error is the type-5 error, voids. Obviously, if all objects were present simultaneously, the O_3 and O_4 objects would be masked by the O_1 and O_2 objects. Also note that, although objects O_1 and O_2 are separated by an angle greater than $\Delta\theta$, they are represented in the PC by a continuum of dots. Then, the two objects would probably be classified not as two distinct objects but as a single larger object (to simplify the representation, the origin of the LiDAR axes has been translated to the bottom-left corner of the figure).

As recently analyzed by Cattini et al. [6], the main effect of axial quantization is to sample and then deform the surrounding environment on concentric spheres whose radii differ by a distance determined by the axial quantization Δr. Given the sampling in spherical coordinates, the axial error is also partly responsible for blurring in the Cartesian representation of the edges of sharp objects. Indeed, as shown in Fig. 1, as the spherical axial coordinate r varies, not only the Cartesian coordinate z varies, but also, in general, the coordinates (x, y) vary, since the (θ_n, φ_m) ray is represented with slightly divergent (x, y) Cartesian coordinates, thus blurring the object edges.

This study focuses on the analysis of the errors and deformations affecting the PC due, on the one hand, to the fact that LiDARs sample the surrounding space along rays angularly spaced of $\Delta\varphi$ and $\Delta\theta$—the angular quantization. On the other hand, due to the fact that, as shown by the reported results, the probability that a ray detects an object can be less than 1, even if the ray completely intercepts the object, as well as it can be greater than 0 even if the ray should not nominally intercept that object. To define the errors in the PC and their probabilities, it is necessary to define what each point of the PC represents. Assuming that a point p in the PC represents an object or a portion of it having the center in p, "vertical" angular extension $\pm\Delta\varphi/2$, and "horizontal" angular extension $\pm\Delta\theta/2$, the angular quantization can give rise to several types of errors, as shown schematically in Fig. 1.

1) *Type-1 Error: Enlargement:* Although the object, or a fraction of it, only partially covers the angular sector of a specific point on the PC, (that is, it does not fully cover the $\pm\Delta\varphi/2$ interval and/or the $\pm\Delta\theta/2$ interval around the point), that point is inserted into the PC. Therefore, in the representation in the PC, the object is enlarged since its angular extension in the PC is greater than the angle under, which it is seen by the LiDAR (e.g., objects O_1 and O_2 in Fig. 1).
2) *Type-2 Error: Shrinkage:* Although the object has an angular extension wider than the angular sampling period, thus affecting at least more than one point in the PC, it is represented in the PC with at least one point less than the affected ones (one less on the right and/or one less on the left, if considering the horizontal dimension and/or one less above and/or one less below if considering the vertical dimension). Therefore, its angular extent in the PC is smaller than the angle under which the object is seen by the LiDAR (e.g., object O_3 in Fig. 1).
3) *Type-3 Error: Shift:* The object is represented in the PC with a point or a set of points whose center is located at different angular coordinates to those of the object center (e.g., objects O_1, O_2, and O_3 in Fig. 1).

As easy to verify, type-1 and -2 errors have a maximum value less than the angular sampling period for each of the object sides (overall, horizontal, and vertical type-1 and -2 errors are always less than twice the respective angular sampling period). Furthermore, type-1 and -2 errors generally imply a type-3 error as well.

In addition to these three errors, a fourth error type may also occur, probably less predictable by the user. According to the definition introduced above, a point p in the PC represents an object or a portion of it, which lies in the angular sector defined by the rectangular base cone centered on the optical axis of the ray under analysis, i.e., at the (θ_n, φ_m) spherical coordinates, and having "vertical" angular extension $\pm\Delta\varphi/2$, and "horizontal" angular extension $\pm\Delta\theta/2$. Therefore, object O_4 in Fig. 1 should not result in a point along the θ_{n+1} ray and, least of all, at a point along the θ_{n+2} or θ_{n+3} rays. Nevertheless, it is important to remember that, when receiving an echo, the LiDAR adds a point in the PC along the optical axis of the considered ray. Thus, if the (θ_n, φ_m) ray samples portions of space also outside the $\pm\Delta\varphi/2$ and $\pm\Delta\theta/2$ rectangular base cone, the PC could report a point along the (θ_n, φ_m) ray even if no object is inside the respective $(\pm\Delta\varphi/2, \pm\Delta\theta/2)$ angular sector. This type of error is the **type-4 error: crosstalk**. Note that, being caused by the fact that LiDAR samples regions of space outside its nominal cone, crosstalk can occur in all LiDAR technologies. For example, if, as shown in Fig. 2, in a scanning LiDAR, the cross section of the beam has an angular extension wider than the angular sampling period $\Delta\theta$, the ray could also reveal an object or portion of it that does not fall within its nominal rectangular base cone—the O object in Fig. 2 revealed by the θ_{n-1} ray. The type-4 error can also occur in flash LiDARs if, due, for example, to optical aberrations or distortions, adjacent pixels collect the echo coming from the same object portion.

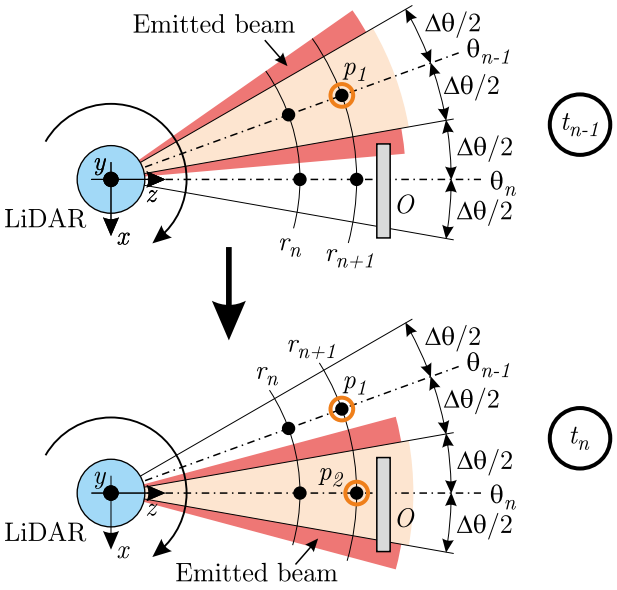

Fig. 2. Schematic of the type-4 error—crosstalk—in scanning LiDARs. At the instant t_{n-1}, the LiDAR emits a beam whose optical axis has nominal azimuth coordinate θ_{n-1}. If, at the object, the angular extension of the emitted beam is greater than the angular sampling period (in the case shown, the horizontal sampling period $\Delta\theta$), the LiDAR can receive an echo even if the object is not present in the angular sector $[\theta_{n-1} - \Delta\theta/2, \theta_{n-1} + \Delta\theta/2]$, thus adding the point p_1 to the PC. At the next instant t_n, the scanning LiDAR emits a beam whose optical axis has nominal azimuth coordinate θ_n. Since the object (O) is present in the angular sector $[\theta_n - \Delta\theta/2, \theta_n + \Delta\theta/2]$, the LiDAR adds point p_2 to the PC.

Note also that, while type-1 and -2 errors may introduce, on each side of the object, an error, which, by definition, is lower than the angular sampling period (the object must at least partially affect the PC point), type-4 error may introduce, on each object side, an error, which can be greater than the angular sampling period (type-4 error implies that the PC reports one or more points that are "external" to the object). Indeed, as will be shown in Section V, especially at close ranges, rays at an angular distance greater than twice the angular sampling period can still detect the object and, thus, represent it in the PC, hence introducing significant deformations.

Finally, if the object involves more rays, the "internal" points of the object image may be missing in the PC

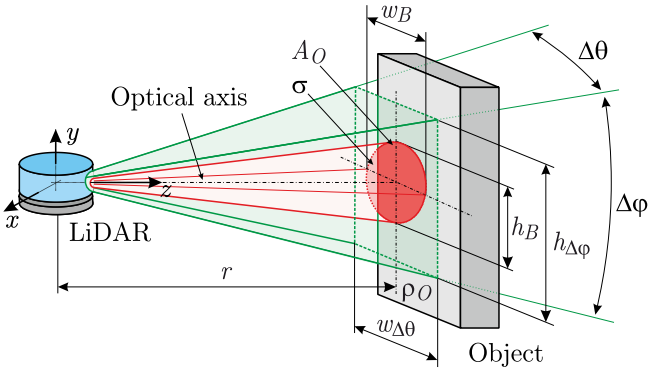

Fig. 3. Out-of-scale representation of the beam incident on the object. The cross section of the beam at the object surface (assumed orthogonal to the optical axis) has a maximum height (dimension along the y-axis) equal to h_B and maximum width (dimension along the x-axis) equal to w_B. σ is the cross-sectional area (projected area) of the beam at the object surface, and A_O is the object area illuminated by the beam ($A_O \subset \sigma$). $w_{\Delta\theta}$ and $h_{\Delta\varphi}$ are the projections of the angular sampling periods $\Delta\theta$ and $\Delta\varphi$ on the object surface. ρ_O is the object reflectance.

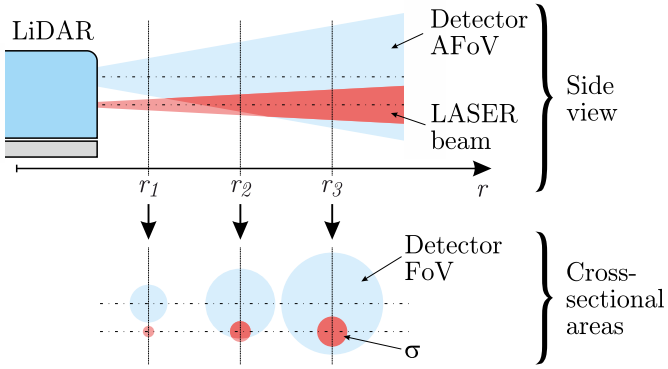

Fig. 4. Schematic of the emission and collection optics of scanning LiDARs. The top figure shows the side view in which it is possible to identify the beam emitted by the LiDAR and the angular field of view (AFoV) of the detector. The bottom figure shows σ, the cross-sectional area of the beam, and the detector field of view (FoV) for three r values. Since the emission and collection optics are not coaxial, at r_1, there is no overlap, therefore, regardless of the object, the reflected echo will not be detected by the LiDAR. At r_2, the overlap is partial; hence, part of the echo will be collected. At r_3, the overlap is complete.

(**type-5 error: voids**). Such an error will be described in more detail in Section IV-B.

The proposed measurement method allows quantifying all these errors both in terms of magnitude and probability as well as allows estimating the effective cross section of the emitted beams (scanning LiDARs), that is, the effective projection of the pixels (flash LiDARs). The impact that such errors and nonidealities will have in terms of, for example, detection, classification, and tracking can be quantified only by considering also the specific algorithms exploited to analyze the PC data to carry out such operations.

III. Theoretical Background

The probability that an echo will give rise to a point in the PC depends on many factors, among which the optical power of the received echo plays a fundamental role [16], [17].

As shown in Fig. 3, the optical power (radiant flux), Φ_R, of the echo received by the detector area A_D after reflection from the (illuminated) object area A_O is given by [18]

$$\Phi_R = \int_{A_O}\int_{A_D} L \cdot \frac{\mathrm{d}a_O \cos\gamma_O \ \mathrm{d}a_D \cos\gamma_D}{l^2} \tag{2}$$

where $\mathrm{d}a_O$ and $\mathrm{d}a_D$ are infinitesimal elements of area on the target and detector surfaces, respectively. l is the distance between $\mathrm{d}a_O$ and $\mathrm{d}a_D$, L is the radiance of the echo at $\mathrm{d}a_O$, and γ_O and γ_D are the angles made by the direction of the flux with respect to the normal to the target and detector surfaces, respectively. The power reaching the detector, thus, depends on many factors, among which [16]: the power Φ_E of the beam emitted by the LiDAR, the angular divergence of the beam (scanning LiDARs), that is, the pixel projection on the object (flash LiDARs), the atmospheric attenuation η_{atm}, the object surface reflectance ρ_O, and the object surface angular dispersion.

The solution of (2) is generally complex and, often, not even possible in an exact way, since many of the parameters are only partially known or unknown. To obtain a model, which, albeit in an approximate way, allows identifying the main quantities determining the power of the received impulse, it is common to approximate the beam emitted by the LiDAR as flat-top and the object surface reflectance as Lambertian. Neglecting other contributions, such as those due to background radiation noise or multiple echos, the power impinging on the detector can be, thus, approximated as follows [17]:

$$\Phi_R = \rho_O \cdot \frac{\Phi_E}{\sigma} \cdot \frac{1}{\pi} \cdot A_O \cdot \frac{A_D}{r^2} \cdot \eta_{\mathrm{atm}}^2 \cdot \eta_{\mathrm{sys}} \tag{3}$$

where, as shown in Fig. 3, ρ_O is the object reflectance and σ is the cross-sectional area of the beam at the object surface (assumed orthogonal to the optical axis of the beam). In (3), $\eta_{\mathrm{atm}}\Phi_E/\sigma$ is, thus, the irradiance incident on the object (flat-top approximation), $\eta_{\mathrm{atm}}\rho_O\Phi_E/\sigma$ is the exitance of the radiation reflected by the object, and $\eta_{\mathrm{atm}}\rho_O\Phi_E/(\sigma\pi)$ is the radiance of the radiation reflected by the object (Lambertian diffuser approximation). Since A_O is the illuminated object area, and A_D/r^2 is the solid angle under which the detector is seen from the object (coaxial epi-illumination approximation), $\eta_{\mathrm{atm}}^2\rho_O\Phi_E A_O A_D/(\sigma\pi r^2)$ is the total radiant flux (power) reflected from the object on the detector area. As previously introduced, η_{atm} is the (single-pass) atmospheric attenuation, whereas η_{sys} is the optical efficiency of the receiver, which considers various aspects of the measuring system.

Note that, as shown in Fig. 4, to avoid power loss due to the beam splitter, in scanning LiDARs, the emitted laser beam is generally not coaxial with the detector's collection optics. This is one of the reasons why η_{sys} typically varies with r, and the optical power Φ_R collected by the LiDAR detector does not simply vary as $1/r^2$ but can instead give rise to more complex and even non-monotonous trends.

IV. Materials and Methods

To investigate the object detection probability and the performances and errors of the LiDAR under test [instrument under test (IUT)], we propose to analyze the "ray detection probability"—the probability that the specific ray adds a point

in the PC. Such a probability is estimated by varying the position of a target object translating it in a direction orthogonal to that of the optical axis of the beam—along the x- or y-axis. For simplicity of discussion, the following description will refer to the analysis of the azimuthal quantization $\Delta\theta$. The method can be easily adapted for the analysis of quantization in the elevation angle, $\Delta\varphi$.

As described in more detail in Section IV-C, the proposed procedure, thus, involves translating a target object and acquiring multiple PCs for each target position. Then, to perform a statistical analysis of how the PC points are distributed among the various bins, such a statistical analysis is the basis of the ray detection probability estimate, which will be described in Section IV-A, and the object detection probability and errors analysis, which will be described in Section IV-B.

Since the PCs are acquired at different instants in time, the random process associated with the object detection must be stationary. The conditions required for the applicability of the proposed method are discussed in Section IV-D.

In the following, Section IV-A describes the data analysis at the basis of the proposed method, Section IV-B proposes a method for estimating the magnitude and probability of errors affecting the PC, and Section IV-C describes in detail the proposed measurement procedure, also reporting the specific settings used to obtain the example results that will be shown in Section V.

Given that, from an operational point of view, the proposed procedure vaguely resembles the knife-edge method used for measuring the divergence of a laser beam, and given that, also, the target object used in the proposed procedure has the shape of a thin sheet of metal, to avoid ambiguity between the generic object and the target object used to estimate the ray detection probability, in the following, the target used to estimate the ray detection probability will be referred to with the term "knife."

A. Estimation of the Empirical Ray Detection Probability

As previously introduced, the proposed procedure analyzes a single beam/pixel—the (θ_n, φ_m) ray—of the IUT exploiting the setup schematically shown in Fig. 5.

The proposed procedure involves fixing the target object (the knife) at the desired distance, d_k, then translating it along the x-axis in steps equal to δ_x acquiring, and analyzing n_{PC} PCs for each knife step. Such an analysis consists in statistically analyzing how the radii, r, of the point along the (θ_n, φ_m) ray are distributed among the various bins—although the PCs are usually supplied in Cartesian coordinates, LiDARs acquire in spherical coordinates as discussed in Section II.

The ray detection probability is, thus, investigated by converting the PC into spherical coordinates, hence analyzing a single ray for each of the acquired PCs. The empirical ray detection probability is, thus, calculated by calculating the ratio between the number of times the point along the ray (θ_n, φ_m) identifies the knife and n_{PC}—the total number of PCs acquired for each knife position. In particular, defining $\Omega(\theta_k, i)$, $i \in [1, n_{\mathrm{PC}}]$, as the set of all points composing the

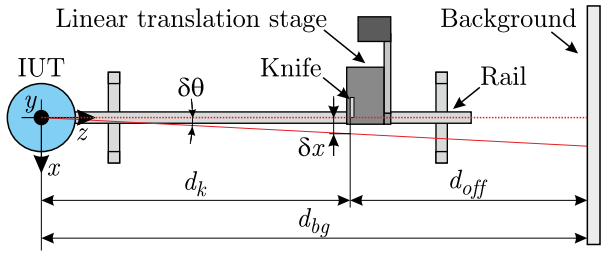

Fig. 5. Out-of-scale representation of the measurement setup. The target object—a thin sheet of painted metal hereinafter referred to as "knife"—is mounted on a linear translation stage that allows translating it along the x-axis of the IUT. d_k is the distance along the z-axis between the knife and the origin of the IUT axes, and $d_{\mathrm{bg}} = d_k + d_{\mathrm{off}}$ is the distance of the origin of the IUT axes from the background being d_{off} the distance between the knife and the background. The displacement of the knife by a quantity δ_x along the x-axis corresponds to a variation of the azimuth angle of the IUT equal to δ_θ. To simplify the alignment between the IUT and the knife, as well as to allow the linear translation stage to be translated along the z-axis to analyze different d_k values, the IUT and the stage are mounted on a rail.

i-th PC acquired by the IUT when the knife edge was at θ_k, the analyzed point was

$$p(\theta_k, i) = \Omega(\theta_k, i) | (\theta = \theta_n, \varphi = \varphi_m). \tag{4}$$

Since the θ and φ values of p are fixed, only the radius, r, can change. As introduced in Section III and described in more detail by Cattini et al. [6], r is a discrete random variable. Therefore, even when the object is correctly detected, the value of r is not a deterministic quantity, but a discrete random variable that can assume the value of the radii of a number of adjacent axial bins. The proposed statistical analysis, thus, involves analyzing the number of times that the p point fell into the set of bins representative of the target object (the knife)

$$p(\theta_k, i) | r \in [r_n - n_b \cdot \Delta r, r_n + n_b \cdot \Delta r] \tag{5}$$

and when, instead, the p point was relative to the background. In (5), r_n is the value of the radius of the bin that best approximates the knife distance d_k, n_b defines the number of bins that are attributed to the correct detection of the target object (the knife), and Δr is the axial quantization step of the IUT. The choice of the value of n_b will be discussed in Section VI.

As described in Section IV-C, the procedure involved analyzing the PCs obtained by translating the knife along the x-axis for both increasing and decreasing x values. In the following, translations in the direction of increasing x will be referred to as clockwise, while those for decreasing values will be referred to as counterclockwise. Defining Λ^+ as the set of the n_{PC} points

$$\Lambda^+(\theta_k) = \{p(\theta_k, 1), p(\theta_k, 2), \ldots, p(\theta_k, n_{\mathrm{PC}})\} \tag{6}$$

obtained once the knife was translated clockwise and the knife edge was at θ_k, the proposed method involves calculating

$$\Gamma^+(\theta_k) = \frac{\mathbf{card}\{\Lambda^+(\theta_k) | r \in [r_n - n_b \cdot \Delta r, r_n + n_b \cdot \Delta r]\}}{\mathbf{card}\{\Lambda^+(\theta_k)\}} \tag{7}$$

where $\mathbf{card}\{\ldots\}$ is the cardinality and $\mathbf{card}\{\Lambda^+(\theta_k)\} = n_{\mathrm{PC}}$.

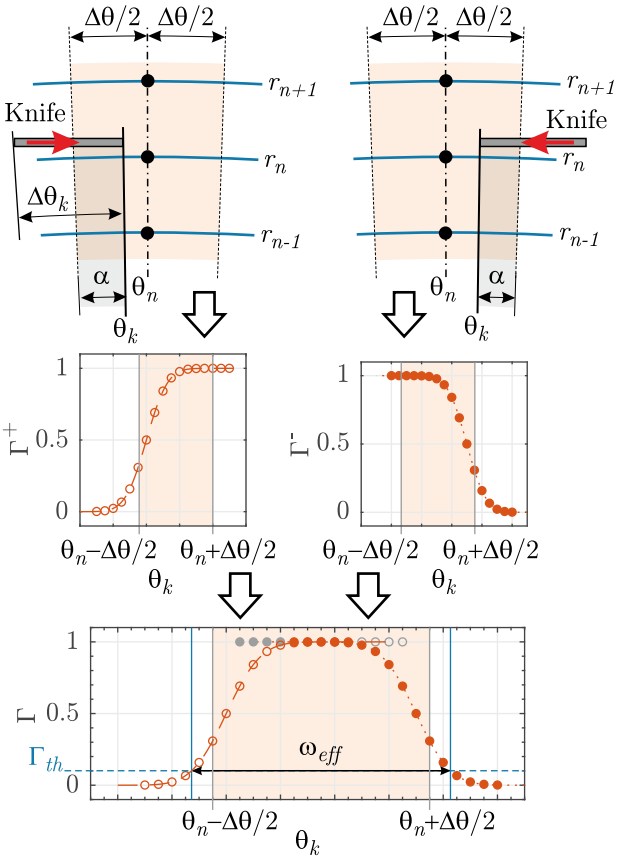

Fig. 6. Schematic of the proposed method. The procedure involves translating the knife along the x-axis for both increasing ("clockwise") and decreasing ("counterclockwise") x values (see Fig. 5). For each knife position, n_{PC} PCs are acquired, and the empirical probabilities $\Gamma^+(\theta_k)$ and $\Gamma^-(\theta_k)$ are calculated as the ratio between the number of times the point along the ray (θ_n, φ_m) identifies the knife and n_{PC}—(7) and (8). θ_k is the azimuth coordinate of the knife edge (right edge for clockwise translation and left edge for counterclockwise translation), while α is the angular extension of the knife within the angular interval relative to the observed ray. Note that, due to crosstalk, α can assume negative values (that is, the ray reveals the knife before it enters its nominal angular sector). $\Delta\theta_k$ is the azimuth angle under which the whole knife is seen by the IUT. From the union of Γ^+ and Γ^-, it is possible to obtain the Γ function as defined in (11). After the definition of a threshold value Γ_{th}, the Γ function allows estimating the effective waist ω_{eff}, that is, the extension of the region around the optical axis in which the object entry entails a detection probability greater than or equal to Γ_{th}.

In the same way, defining $\Lambda^-(\theta_k)$ as the set of all p points obtained from the n_{PC} measures acquired by translating the knife counterclockwise, the proposed method involves also calculating

$$\Gamma^-(\theta_k) = \frac{\mathbf{card}\{\Lambda^-(\theta_k) | r \in [r_n - n_b \cdot \Delta r, r_n + n_b \cdot \Delta r]\}}{\mathbf{card}\{\Lambda^-(\theta_k)\}}. \tag{8}$$

From Figs. 1 and 6, it is easy to observe that $\Gamma^+(\theta_k)$ is the empirical probability that the (θ_n, φ_m) ray will detect an object located to the left of the optical axis of the beam and whose right edge is at $(\theta_n - \Delta\theta/2 + \alpha)$. In the same way, $\Gamma^-(\theta_k)$ is the empirical probability the (θ_n, φ_m) ray will detect an object located to the right of the optical axis of the beam and whose left edge is at $(\theta_n + \Delta\theta/2 - \alpha)$.

Assuming that the ray detection probability is symmetrical with respect to the optical axis of the (θ_n, φ_m) ray, it is possible to define the mean empirical object detection probability

$$\bar{\Gamma}(\alpha) = [\Gamma^+(\alpha) + \Gamma^-(\alpha)]/2 \tag{9}$$

where, as shown in Fig. 6

$$\alpha = \begin{cases} \theta_k - (\theta_n - \Delta\theta/2), & \text{for clockwise translation} \\ (\theta_n + \Delta\theta/2) - \theta_k, & \text{for counterclockwise translation} \end{cases} \tag{10}$$

is the angular extension of the knife within the nominal angular interval relative to the observed ray. Note that, in the presence of crosstalk, $\bar{\Gamma}(\alpha)$ can be greater than zero even for negative α values. As shown in Fig. 6, from the empirical probabilities $\Gamma^+(\theta_k)$ and $\Gamma^-(\theta_k)$, it is also possible to define the function

$$\Gamma(\theta_k) = \min\{\Gamma^+(\theta_k), \Gamma^-(\theta_k)\}. \tag{11}$$

As described in more detail in the following sections, the $\Gamma(\theta_k)$ function allows, on the one hand, to realize graphs capable of providing an intuitive representation of the IUT behavior and, on the other, to define the effective beam waist ω_{eff}. Note that if ω_{eff} exceeds $w_{\Delta\theta}$ (the projections of the angular sampling periods $\Delta\theta$—see Fig. 3), the (θ_n, φ_m) ray overhangs the adjacent ray; thus, there is crosstalk (error 4). This aspect will be discussed in greater detail in the next sections.

Equation (11) was also used to define the position of the knife within the LiDAR reference system—θ_k. Under the hypothesis that the ray detection probability is symmetrical to the optical axis of the (θ_n, φ_m) ray, θ_n is at the center of the $\Gamma(\theta_k)$ curve. Therefore, since the knife distance, d_k, and the translation step amplitude, δ_x, are known, once the Γ curve has been constructed, for each of the acquisitions, it is possible to estimate the knife position in the LiDAR reference system, θ_k, imposing that the center of gravity of the curves was in correspondence of the ray optical axis.

Note that different rays can have different performances, thus different $\bar{\Gamma}(\alpha)$ and $\Gamma(\theta_k)$ functions. Nevertheless, the proposed procedure can be easily repeated for the characterization of all rays of interest.

B. Estimation of the Object Detection Probability and Errors

As shown in Fig. 7, an object can extend over several rays. Thus, depending on parameters such as its distance and reflectance (Section III), its detection by the LiDAR can occur with a different number of points in the PC, resulting in one or more of the errors described in Section II.

As introduced in Section IV-A and discussed in more detail in Sections IV-C and VI, $\bar{\Gamma}(\alpha)$ represents the ray detection probability relative to an object having dimensions greater than or equal to those of the used knife and extending in the considered ray for an angle α. For internal rays, the $\{j+1, j+2, \ldots, j+N_\theta-2\}$ in Fig. 7, the object covers the entire angular sector. Thus, assuming that the vertical extension of the object is such as to completely cover the entire $[\varphi_m - \Delta\varphi/2, \varphi_m + \Delta\varphi/2]$ angular sector and, assuming, for simplicity of discussion, that vertical crosstalk is negligible (note that, in general, $\Delta\varphi \gg \Delta\theta$), the ray detection probability relating to an internal ray is equal to

$$\Psi_{\mathrm{int}}(r) = \bar{\Gamma}(\Delta\theta, r) \tag{12}$$

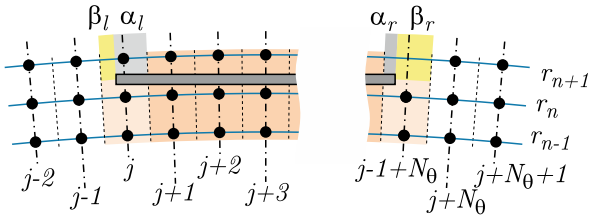

Fig. 7. Schematic of the object sampling by the LiDAR (single elevation angle φ_m). The object dimensions are such to involve N_θ rays. For internal rays, $\{j+1, j+2, \ldots, j+N_\theta-2\}$, the sectors represented in dark orange color, the object completely covers the $\pm\Delta\theta/2$ range. For the two rays intersecting the object edges—the outer rays $\{j, j+N_\theta-1\}$ represented in the figure with the light orange color—the coverage can be partial. If crosstalk is present, even rays whose nominal cone does not intersect the object, i.e., external rays, such as $\{\ldots, j-2, j-1, j+N_\theta, j+N_\theta+1, \ldots\}$, can still give rise to a point in the PC. In the figure, the left object edge extends into the j-ray by an angle $\alpha=\alpha_l$, while the right edge extends into the $(j+N_\theta-1)$ ray by an angle $\alpha=\alpha_r$. $\beta_l=\Delta\theta-\alpha_l$, $\beta_r=\Delta\theta-\alpha_r$, and $\beta=\beta_l+\beta_r$.

where $\bar{\Gamma}(\Delta\theta, r)=\bar{\Gamma}(\Delta\theta, r, \theta_n, \varphi_m)$ is the $\bar{\Gamma}$ function of the considered (θ_n, φ_m) ray for $\alpha=\Delta\theta$ and an object distance r. Equation (12) neglects the contribution due to the possibility that the considered ray samples regions of space also for $\alpha>\Delta\theta$. This occurs when crosstalk is present. However, in the presence of crosstalk, it is reasonable to assume that already $\bar{\Gamma}(\Delta\theta)$ saturates at 1. Hence, neglecting the contribution for $\alpha>\Delta\theta$ makes it possible to greatly simplify the analytical treatment without introducing significant errors.

For the two rays intersecting the object edges, the outer rays $\{j, j+N_\theta-1\}$ in Fig. 7, the object extends for an angle whose value depends on the size and distance of the object. An object seen by the LiDAR under an azimuth angle ξ affects a number of rays

$$N_\theta(\xi)=\left\lfloor\frac{\xi}{\Delta\theta}\right\rfloor+1 \tag{13}$$

where $\lfloor x\rfloor$ is the rounding down (or floor function) of x—the largest integer less than or equal to x (since the object edge generally does not coincide with the beginning of the angular sector of a ray, the rounding down plus 1 allows considering the case in which the object is an integer multiple of the sampling period). As shown in Fig. 7, in each of the two object sides ("outer" rays), the value of α cannot be less than

$$\alpha_{\text{MIN}}(\xi)=\Delta\theta-\beta=\xi-\{[N_\theta(\xi)-1]\cdot\Delta\theta\}. \tag{14}$$

Thus, assuming that the object can be found within the N_θ rays interval with equal probability (uniform random variable), for the two rays relative to the object edges (outer rays), the ray detection probability is equal to

$$\Psi_{\text{out}}(r)=\frac{1}{\Delta\theta-\alpha_{\text{MIN}}}\cdot\int_{\alpha_{\text{MIN}}}^{\Delta\theta}\bar{\Gamma}(\alpha, r)\ \mathrm{d}\alpha. \tag{15}$$

Also, in this case, $\bar{\Gamma}(\alpha, r)$ and, therefore, $\Psi_{\text{out}}(r)$ can be a function of the considered (θ_n, φ_m) ray.

For the first of the external rays, that is, the two adjacent to the outer rays, the edge of the object is at $\alpha\in[\Delta\theta-\alpha_{\text{MIN}}, 0)$. Thus, assuming again that the object can be found within the N_θ rays interval with equal probability (uniform random variable), the ray detection probability for the first of the external rays (the $j-1$ and $j+N_\theta$ rays in Fig. 7) is equal to

$$\Psi_{\text{ext}_1}(r)=\frac{1}{\Delta\theta-\alpha_{\text{MIN}}}\cdot\int_{-\Delta\theta+\alpha_{\text{MIN}}}^{0}\bar{\Gamma}(\alpha, r)\ \mathrm{d}\alpha. \tag{16}$$

In general, the ray detection probability for the i-th external ray is equal to

$$\Psi_{\text{ext}_i}(r)=\frac{1}{\Delta\theta-\alpha_{\text{MIN}}}\cdot\int_{-i\cdot\Delta\theta+\alpha_{\text{MIN}}}^{-(i-1)\cdot\Delta\theta}\bar{\Gamma}(\alpha, r)\ \mathrm{d}\alpha. \tag{17}$$

$\Psi_{\text{ext}_1}(r)$ and $\Psi_{\text{ext}_i}(r)$ can also be a function of the of the considered (θ_n, φ_m) ray.

Given that non-detection and detection are mutually exclusive and exhaustive events, and assuming that the rays detection probabilities are independent random variables, the probability that an object is reconstructed with all and only the rays belonging to a certain set of rays Ξ is given by

$$P_\Xi(r)=\left[\prod_{\text{ray}\ \in\ \Xi}\Psi(r)\right]\cdot\left\{\prod_{\text{ray}\ \notin\ \Xi}[1-\Psi(r)]\right\} \tag{18}$$

where, depending on whether the ray is internal, outer, or external, its ray detection probability $\Psi(r)$ can be calculated using equations (12), (15), or (17). In the case in which at the specific distance r the crosstalk is negligible or in the case in which only interested in the rays belonging to the set Ξ and not also in the other rays composing the PC, it is possible to omit the second product in (18).

Even omitting the second product, the solution of (18) can be significantly laborious. In this regard, it is useful to consider that the objects that are often more difficult to detect are the "small" ones, that is, those involving a limited number of adjacent rays. Especially, for adjacent rays, it is reasonable to assume that the $\bar{\Gamma}$ functions are extremely similar, if not identical. Hence, assuming that all the rays have the same $\bar{\Gamma}(\alpha, r)$ and that such detection probabilities are independent random variables, it is possible to significantly simplify the solution. For example, in the case of the validity of the previous simplifying hypotheses, the probability that the LiDAR reveals the object representing it in the PC with at least all the $N_\theta-2$ internal rays plus the two outer rays is given by

$$P_{1_{\text{ALL}}}(r)=[\Psi_{\text{int}}(r)]^{N_\theta-2}\cdot[\Psi_{\text{out}}(r)]^2. \tag{19}$$

If interested not only in the fact that the object is reconstructed in the PC with all internal and outer points but also that none of the external points represent the object, the probability becomes

$$P_{1_{\text{ALL and ONLY}}}(r)=P_{1_{\text{ALL}}}(r)\cdot\prod_{i=1}^{\infty}[1-\Psi_{\text{ext}_i}(r)]^2. \tag{20}$$

The (angular) error (type-1 error, enlargement) made by the LiDAR in reconstructing the object in case it is represented it in the PC with all and only the $N_\theta-2$ internal rays plus the two outer rays would be equal to

$$\epsilon_{1_{\text{ALL and ONLY}}}=N_\theta\cdot\Delta\theta-\xi. \tag{21}$$

Such a type-1 error would also correspond to a type-3 error (shift, $\epsilon_{3_{\text{ALL}}}$) equal to the difference between the position of the N_θ rays center and the object center position. Given the hypothesis that the object can be found within the N_θ rays with equal probability, the mean value of this error is zero, while the magnitude of the maximum value is equal to

$$\max\{\epsilon_{3_{\text{ALL}}}\} = (\Delta\theta - \beta)/2. \tag{22}$$

The probability of the most extreme type-2 error (shrinkage), that is, the one in which none of the internal, outer, and external rays reveal the object, can be easily calculated as follows:

$$P_{2_{\text{NONE}}}(r) = [1 - \Psi_{\text{int}}(r)]^{N_\theta - 2} \cdot [1 - \Psi_{\text{out}}(r)]^2 \cdot \cdot \prod_{i=1}^{\infty} [1 - \Psi_{\text{ext}_i}(r)]^2. \tag{23}$$

Proceeding in the same way, it is possible to calculate the probabilities of any other combination and the magnitude of the related error.

For example, the probability that all internal rays will detect the object and that neither of the two outer rays will reveal the object is equal to

$$P_{2_{\text{NoOuter}}}(r) = [\Psi_{\text{int}}(r)]^{N_\theta - 2} \cdot [1 - \Psi_{\text{out}}(r)]^2. \tag{24}$$

Similar to before, if interested in whether none of the external points also represent the object, the probability becomes

$$P_{2_{\text{NoOuterNoExternal}}}(r) = P_{2_{\text{NoOuter}}}(r) \cdot \prod_{i=1}^{\infty} [1 - \Psi_{\text{ext}_i}(r)]^2. \tag{25}$$

The error relative to $P_{2_{\text{NoOuterNoExternal}}}$ is

$$\epsilon_{2_{\text{NoOuterNoExternal}}} = (N_\theta - 2) \cdot \Delta\theta - \xi. \tag{26}$$

The probability that a crosstalk error occurs (error 4), such that the LiDAR reveals the object representing it in the PC with all and only the N_θ rays plus both the two first external rays, is

$$P_{4_{\text{sides}}} = P_{1_{\text{ALL}}} \cdot [\Psi_{\text{ext}_1}(r)]^2 \cdot \prod_{i=2}^{\infty} [1 - \Psi_{\text{ext}_i}(r)]^2 \tag{27}$$

and the respective angular error (type-4 error, crosstalk) made by the LiDAR is

$$\epsilon_{4_{\text{sides}}} = (N_\theta + 2) \cdot \Delta\theta - \xi. \tag{28}$$

Given that error 5 is the lack of one of the points relating to the internal rays, the probability of the type of error 5 in which at least 1 of the $N_\theta - 2$ points relating to the internal rays is missing is equal to

$$P_{5_{\text{AtLeastOne}}} = 1 - [\Psi_{\text{int}}(r)]^{N_\theta - 2}. \tag{29}$$

Similarly, the probability that one internal ray is missing, while all the other $N_\theta - 3$ internal rays report a point in the PC, is

$$P_{5_{\text{One}}} = [\Psi_{\text{int}}(r)]^{N_\theta - 3} \cdot [1 - \Psi_{\text{int}}(r)]. \tag{30}$$

Proceeding in the same way, it is possible to calculate all the other detection probabilities and related errors.

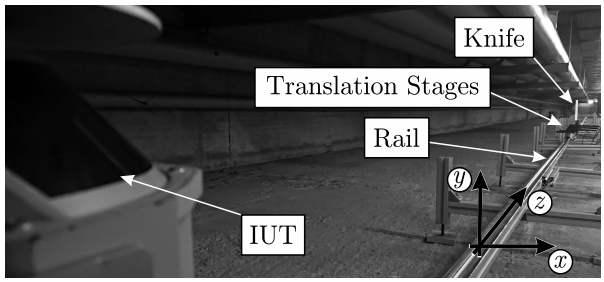

Fig. 8. Picture of the experimental setup. To avoid potential interference from the rail, the LiDAR is positioned at a height to the ground (y-axis) greater than that of the rail. Thus, only the upper part of the knife falls within the space sampled by the LiDAR (see Fig. 12). To make the knife more visible, a vertical white line has been added to the figure, and to simplify the representation, the origin of the LiDAR axes has been translated to the bottom-right corner of the figure.

C. Measurement Procedure

As previously introduced, the proposed procedure analyzes a single ray exploiting the setup schematically represent in Fig. 5 and shown in Fig. 8. The "knife" has to be mounted on a linear translation stage to finely translate it along the x-axis of the IUT. Given the possibility of error 4 (crosstalk), the scanned area must be wider than $[\theta_n - \Delta\theta/2, \theta_n + \Delta\theta/2]$ range. As an example, the results reported in Section V were obtained using a stack of three motorized linear translators model Z825B by Thorlabs.

To minimize the effect due to any inclination of the knife to the direction orthogonal to the beam radius, the knife must be thin—the thickness t_k along the z-axis must be much less than the width along the x-axis. Similarly, given that, for simplicity of discussion, the description refers to the analysis of the azimuthal quantization $\Delta\theta$, the knife must have a dimension along the y-axis, the height h_k, such as to go beyond the $[\varphi_m - \Delta\varphi/2, \varphi_m + \Delta\varphi/2]$ interval. In general, the vertical sampling period, $\Delta\varphi$, is significantly larger than the horizontal sampling period $\Delta\theta$. Hence, vertical crosstalk is less likely. Nevertheless, it is convenient to use a knife with a vertical dimension such as to be seen by the LiDAR under an elevation angle significantly greater than $\Delta\varphi$, for example, $3\Delta\varphi$.

The choice of the knife width w_k—its dimension along the x-axis—plays a fundamental role and will be discussed in more detail below.

Once the linear translation stages have been fixed at the desired working distance d_k and waited for the system warm-up, n_{PC} PCs have to be acquired for each knife edge position. As previously discussed, the procedure should be repeated by translating the knife clockwise and counterclockwise. As evident from Fig. 6, if the clockwise translation is large enough, the left edge of the knife samples the same positions it would have sampled during the counterclockwise translation. Therefore, the clockwise translation can also be used for the estimate of Γ^-. The possibility of sampling without having to disassemble and reassemble the knife allows obvious advantages in terms of uncertainty in the repositioning and duration of acquisitions.

Once the scanning at the d_k distance is completed, the knife has to be moved to the next axial distance, and the procedure has to be repeated.

As previously introduced, the knife width w_k plays a fundamental role. In theory, just as h_k must be such as to guarantee that it can cover the entire $\pm\Delta\varphi$ interval (plus any vertical crosstalk), w_k should also be such as to guarantee that it can cover the entire angular sector $[0, \Delta\theta]$ plus any horizontal crosstalk—$\Delta\theta_k \geq \Delta\theta$ (see Fig. 6). Using a knife of such a width with the possibility of avoiding disassembling and reassembling it between clockwise and counterclockwise acquisitions (thus avoiding the associated uncertainty) requires translation stage/s with a travel that, as the distance of the knife increases, can become significantly wide.

As reported in Section III, the detection probability increases as the optical power Φ_R collected by the detector increases. Therefore, reducing the knife area generally implies the risks of reducing the power Φ_R, hence, the relative ray detection probability. Nevertheless, the detection probability cannot exceed the value of 1. Therefore, when the received power exceeds a certain value, the ray detection probability no longer increases, as the power Φ_R increases. In other words, for each knife position, it is possible to reduce the w_k width until the received power is such as to give rise to a detection probability of 1.

Assuming that the power collected by the detector increases, as the object approaches the optical axis of the ray, it would theoretically be possible to use a knife with a width such as to be seen by the LiDAR under an azimuth angle

$$\Delta\theta_{k-\mathrm{MIN}}(r) = \alpha_1(r) - \alpha_0(r) \tag{31}$$

where

$$\begin{aligned} \alpha_0(r) &= \min\{\alpha \in [-\infty, \Delta\theta] \mid \bar{\Gamma}(\alpha, r) > 0\} \\ \alpha_1(r) &= \min\{\alpha \in [-\infty, \Delta\theta] \mid \bar{\Gamma}(\alpha, r) = 1\}. \end{aligned} \tag{32}$$

α_0, thus, represents the angle at which the ray begins to detect the object, and $\alpha_1 - \alpha_0$ is the minimum object angular extension that gives rise to a ray detection probability of 100%. Note that, due to crosstalk, both α_0 and α_1 can take the negative values. Moreover, as $\bar{\Gamma}(\alpha)$ is a function of the distance r, so are $\Delta\theta_{k-\mathrm{MIN}}$, α_0, and α_1. For some r values, $\bar{\Gamma}(\alpha)$ may never reach the value of 1. In this case, since the $\bar{\Gamma}(\alpha)$ function is monotone increasing, α_1 is the smallest α value for which the $\bar{\Gamma}(\alpha)$ function reaches its maximum.

Using a knife of angular dimension $\Delta\theta_k = \Delta\theta_{k-\mathrm{MIN}}$ not only reduces the travel required to the translation stage to collect both Γ^+ and Γ^- without having to disassemble and reassemble the knife but also allows obtaining more information. As described in more detail in Section VI, the angle under which the IUT sees the knife also defines the minimum angular dimension of the object for which the proposed method can provide the full estimate of the ray detection probability and, therefore, of the object detection probability.

The example results that will be shown in Section V have been obtained by exploiting a knife composed of a thin sheet of steel having $h_k = 400$ mm, $w_k = 10.0$ mm, and $t_k = 0.7$ mm.

As described in Section III, the object reflectance plays a role in the optical collected power and, therefore, in the object detection. To know the reflectance value of the knife, it was painted with white paint having known reflectance ($\rho_O = 75\%$ at the IUT wavelength).

Tests were performed in a controlled environment where both temperature and lighting were monitored. Moreover, to avoid the background could affect the results [19], measurements were performed setting $d_{\mathrm{bg}} > 100$ m (see Fig. 5).

D. Conditions Required for the Applicability of the Proposed Method

As previously introduced, since the various PCs are acquired at different instants in time, the random process associated with the object detection must be stationary. It is, therefore, necessary to evaluate both the warm-up and the stability "over time" of the measuring system. Moreover, for the proposed method to be applicable, for each knife position, it is necessary to be able to acquire n_{PC} PCs under the repeatability condition of measurement. It is, therefore, necessary that the IUT is stable also in space; that is, each of the sets of acquired PCs must analyze exactly always the same set of elevation and azimuth angles—the same spherical coordinates θ and φ. Such a condition is intrinsically guaranteed in flash LiDARs (as the observation directions are defined by the detector array), and it is generally substantially guaranteed also for scanning LiDARs based on MEMS and optical phase arrays (OPAs) technologies. For spinning LiDARs, such must be verified. If the LiDAR does not always sample along the same azimuth and/or elevation angles, the ray detection probability could still be estimated by selecting and analyzing only the PCs containing the ray of interest—(θ_n, φ_m). However, if the LiDAR does not always sample along the same angles, the estimation of the probabilities and errors reported in Section IV-B would become more complex.

To verify the space-time stability of the IUT, we, thus, propose to follow the procedure previously described by Cattini et al. [6]. Therefore, to acquire PCs with a sampling period equal to that with which the PCs used to estimate the ray detection probability are obtained and for a time long enough to reasonably cover both the warm-up and the time needed to perform knife-edge measurements—it is necessary to obtain an estimate of the temporal stability for a period of no less than to warm-up plus the time required to perform knife-edge measurements. Then, it is necessary to verify that the azimuth and elevation angles observed by the IUT remain constant. Such can be performed by simply analyzing the PCs in spherical coordinates. If it is confirmed that the IUT always samples the same nominal spherical coordinates θ and φ, it is possible to proceed to the temporal stability analysis. As described in more detail by Cattini et al. [6], such can be performed by statistically analyzing how the points distributed in the various bins as time t changed and, in particular, to analyze it with movable time windows having a width equal to n_{PC} multiplied by the number of knife positions that are analyzed for each knife distance d_k.

V. Example Results

To provide an idea of the results that can be obtained by exploiting the proposed method, this section contains examples acquired by investigating the LiDAR model MRS 6000 by

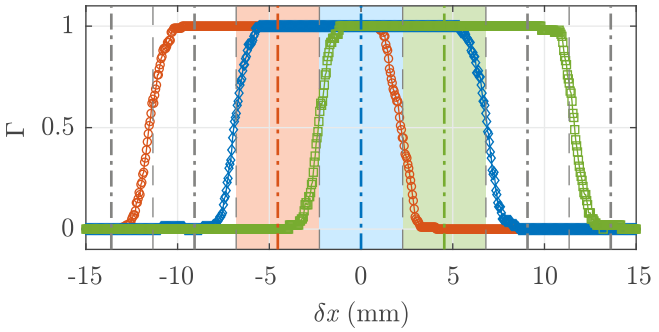

Fig. 9. Γ functions obtained from three adjacent rays—θ_{n-1}, θ_n, and θ_{n+1}—at a knife distance $r = 2$ m. The vertical dashed lines represent the angular sectors of width $\pm\Delta\theta/2$, and the dashed-dotted lines represent the optical axes of the rays.

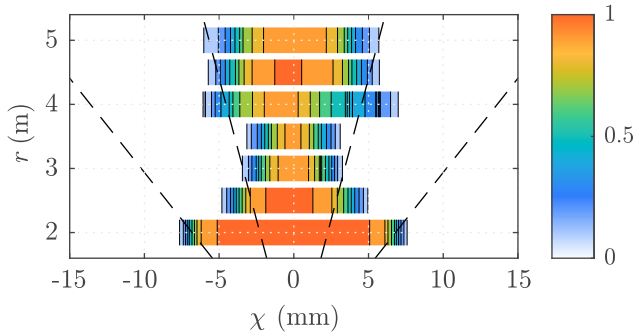

Fig. 10. Γ_{mean} function as a function of the object distance r. The oblique dashed lines represent the angular sectors of width $\pm\Delta\theta/2$ centered on the ray optical axes.

SICK. Since the proposed method focuses on the experimental determination of the ray detection probability, the reported examples will focus on this aspect and on the type of error that is probably the most unexpected, i.e., the crosstalk.

Fig. 9 shows an example of the Γ functions for three adjacent rays—θ_{n-1}, θ_n, and θ_{n+1}.

To provide a summary representation of the results obtained, Fig. 10 shows the Γ_{mean} function as a function of the object distance r. The $\Gamma_{\text{mean}}(\chi, r)$ function was calculated as the mean of the three adjacent rays

$$\Gamma_{\text{mean}}(\chi, r) = \frac{1}{3}\sum_{i=n-1}^{n+1} \Gamma_{\theta_i}(\chi, r) \tag{33}$$

where χ is the distance along the x-axis from the ray optical axis (the dashed-dotted lines in Fig. 9), and $\Gamma_{\theta_i}(\chi, r)$ is the Γ function relative to the θ_i ray. Fig. 11 shows the respective experimental standard deviation of the mean

$$\sigma_\Gamma(\chi, r) = \sqrt{\frac{1}{3\cdot 2}\sum_{i=n-1}^{n+1} [\Gamma_{\theta_i}(\chi, r) - \Gamma_{\text{mean}}(\chi, r)]^2}. \tag{34}$$

As expected from Fig. 9, at the distance $r = 2$ m, the experimental standard deviation of the mean, σ_Γ, is equal to zero for many χ values. In fact, as can be seen from Fig. 9, at the $r = 2$ m distance, all three functions Γ remain substantially equal to 1 for $\chi \in [-5.5, 5.5]$ mm. All the Γ functions obtained from the θ_{n-1}, θ_n, and θ_{n+1} rays are reported in the Appendix.

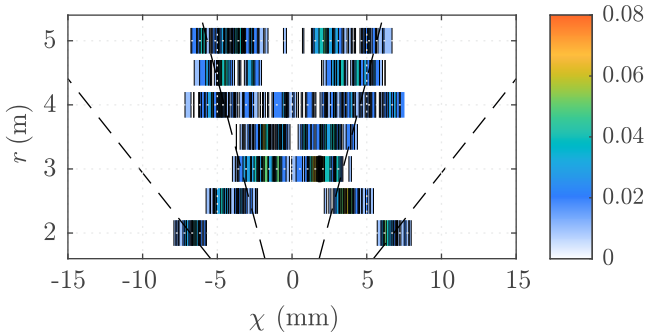

Fig. 11. Experimental standard deviation of the mean, $\sigma_\Gamma(\chi)$, as a function of the object distance r. The oblique dashed lines represent the angular sectors of width $\pm\Delta\theta/2$ centered on the ray optical axes.

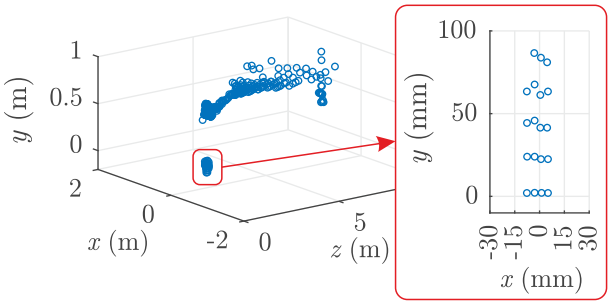

Fig. 12. PC obtained by positioning a thin object (width approximately 3.5 mm) at a distance of 2 m from the LiDAR. The object was painted using the same paint used to cover the knife. Although the object is seen by the LiDAR under an azimuth angle less than the azimuth sampling period $\Delta\theta$, the object is reconstructed in the PC with four adjacent points confirming the crosstalk, thus confirming what was predicted by Figs. 9 and 10. Note that, since the LiDAR samples the environment on concentric spheres whose radii differ by Δr, if the points of the PC are at different radial distances (different bins), the same elevation angle φ_m gives rise to slightly different y values.

As previously shown in Fig. 6, once defined the detection probability of interest—the threshold value Γ_{th}—Fig. 10 allows estimating the effective waist ω_{eff} as the distance to the object changes. For example, the value of ω_{eff} obtained by imposing $\Gamma_{\text{th}} = 0.2$ represents the extension of the region around the optical axis in which the object entry entails a detection probability greater than or equal to 20%. According to (3), the ω_{eff} varies with the object distance. Due to η_{sys}, the observed trend is not monotonous.

From Figs. 9 and 10, it is evident the presence of crosstalk for an object distance of about 2 m.

As an example, Fig. 12 shows the PC obtained by positioning, at a distance of 2 m, a thin object (width approx. 3.5 mm) painted using the same paint used to cover the knife. As expected from Figs. 9 and 10, although the object is seen by the LiDAR under an azimuth angle less than the azimuth sampling period $\Delta\theta$, the object is reconstructed in the PC with four adjacent points confirming the crosstalk. Thus, an object whose size is about 3.5 mm is represented in the PC with a width of about 18.5 mm, that is, more than five times wider.

VI. Discussion

For simplicity of discussion, the description of the proposed method referred to the analysis of the azimuthal quantization $\Delta\theta$. The method can be easily adapted for the analysis of

quantization in the elevation angle, $\Delta\varphi$. Nevertheless, whether analyzing the effect of the azimuthal quantization or that relating to the elevation angle, at present, the proposed method requires a minimum object size along the direction defined by the other spherical angle. Therefore, in the case of analyzing the effect of quantization in the azimuthal angle, the proposed analysis is based on the hypothesis that the object has a vertical extension, such as to cover the entire angular sector of amplitude $\Delta\varphi$ (plus any vertical crosstalk). Indeed, in ground-based applications, objects often have vertical development; thus, the smallest size is typically the width. Nevertheless, the proposed method can be easily adapted to analyze the effect of vertical quantization (in this second case, the object would be translated along the y-axis and should cover the entire angular sector $\pm\Delta\theta/2$ plus any horizontal crosstalk). Finally, using a knife, which, in addition to being translated in the horizontal direction, is also raised, it would be possible to obtain an estimate, albeit approximate, of the joint effect of the horizontal and vertical quantizations.

It is important to notice that the obtained results are based on the hypothesis that a point p in the PC represents an object or portion of an object having the center in p, "vertical" angular extension $\pm\Delta\varphi/2$, and "horizontal" angular extension $\pm\Delta\theta/2$. Such a partition of the 3-D image into rectangular base cones serves only to define what the points of the PC represent, thus serving as a starting point for the definition of the errors. As shown by the reported results, in general, this partition does not fully coincide with the spatial sampling actually performed by LiDAR. Indeed, due to phenomena, such as the divergence of the beam and possible aberrations of the collection optics, as well as due to the discrimination threshold of the detector, the actual spatial region within which the ray samples the surrounding space may be greater than or even smaller than the nominal rectangular base cone giving rise, on the one hand, to phenomena, such as crosstalk, and on the other, the missed detection of the object. A different definition of what point p represents would lead to a redefinition of the related errors. Nevertheless, the procedure proposed in Section IV-B for estimating the errors is simple, and it would, therefore, be quite simple to adapt it to a different definition.

As described in Section IV-C, $\bar{\Gamma}(\alpha)$ represents the probability of detecting an object having dimensions greater than or equal to those of the used knife and extending in the considered ray for an angle α. Since $\bar{\Gamma}$ is a function bounded above, it is, thus, theoretically possible to use a knife seen by the LiDAR under an angle $\Delta\theta_{k-\mathrm{MIN}}(r) \leq \Delta\theta_k$. If $\Delta\theta_k < \Delta\theta$, $\bar{\Gamma}$ not only represents the probability of detecting an object extending from one of the ray edges by an angle α but also the probability of detecting an object of angular amplitude $\Delta\theta_k$ whose center is at an angular distance from the axis optical equal to

$$(\Delta\theta - 2\alpha - \Delta\theta_k)/2. \tag{35}$$

If the object of interest is seen by the LiDAR under an angle lower than the value of $\Delta\theta_k$ used for its characterization, the estimate provided by $\bar{\Gamma}$ is valid only as long as $\alpha \leq \Delta\theta_k$, while it can be an overestimate when α exceeds such a value.

The proposed method also allows obtaining an estimate of the LiDAR lateral resolution. Indeed, it is statistically unlikely that the LiDAR distinguishes two objects [of angular dimension greater than or equal to $\Delta\theta_{k-\mathrm{MIN}}(r)$] that are angularly separated by an angle less than or equal to

$$\psi(r) = \max\{[\Delta\theta - \alpha_1(r)], [\Delta\theta - 2\alpha_1(r)]\} \tag{36}$$

where, as defined in (32), α_1 is the minimum value of α for which $\bar{\Gamma}(\alpha) = 1$. Indeed, objects separated by an angular distance less than $\psi(r)$ statistically give rise to a continuum of points in the PC. Note that, as shown in Figs. 9 and 10, α_1 can be significantly less than 0, and therefore, ψ can be significantly greater than the "resolution" ($\Delta\theta$) declared by the manufacturer.

Driven by market demands of 3-D LiDARs for 3-D object perception and scene segmentation, LiDAR manufacturers are nowadays proposing measuring systems that claim better and better resolutions day by day. Especially, for LiDAR in scanning technology, this clashes with the intrinsic nonidealities of the measurement principle, thus potentially leading to significant crosstalk. Indeed, the race to an ever-smaller angular sampling period can cause the beam emitted by the LiDAR to be wider than the solid angle defined angular sampling periods (see Fig. 3). This can lead to significant crosstalk. Small objects that should have given rise to a few points in the PC can, thus, be deformed and enlarged on a significantly greater number of points, as shown in Fig. 12. Likewise, objects angularly separated by an angle greater than the sampling angle can unexpectedly result in a continuum of points in the PC—see (36). Such errors may compromise the effective ability of the system to perform very important tasks, such as detection, classification, and tracking.

Note, however, that the proposed method has the sole objective of allowing obtaining a statistical estimate of the errors that will affect the LiDAR output—the PC. The impact that such errors could generate in the subsequent processing system in terms of, for example, detection, classification, and tracking, depends inexorably on the specific algorithms exploited by the processing system. For example, focusing on a single channel and assuming that only one point is sufficient to detect the object, its object detection probability is equal to $1 - P_{2_{\mathrm{NONE}}}$. Similarly, as discussed above, if two objects are separated by an angle less than $\psi(r)$, they will statistically give rise to a continuum of points in the PC. Thus, it is reasonable to assume that the algorithm used for the classification will identify the two objects as a single object. Based on what the specific classification algorithm used to distinguish two objects requires, it is possible to estimate the probability of this event by proceeding in a similar way to what was done in Section IV-B.

It is also important to note that the obtained estimates depend on factors such as the object reflectance and the uncertainty admitted in the estimate of the axial coordinate. Therefore, on the one hand, a knife with a reflectance as similar as possible to that of the object of interest must be used (the example results shown in Section V have been obtained using a knife with $\rho_O = 0.75$). On the other hand, the n_b value must be appropriately chosen. Indeed, the product $n_b \cdot \Delta r$

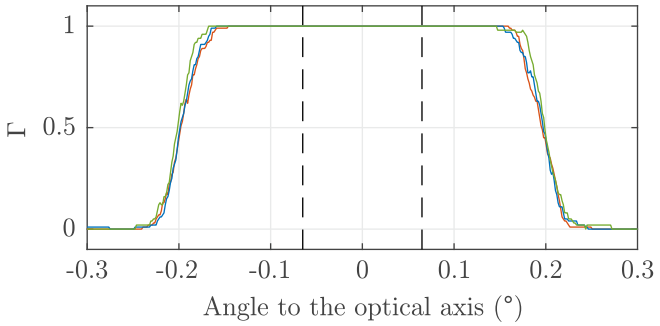

Fig. 13. Γ functions of the θ_{n-1}, θ_n, and θ_{n+1} rays as a function of the angular distance from the ray optical axis obtained at $r = 2$ m distance. The dashed lines represent the angular sectors of width $\pm\Delta\theta/2$ centered on the ray optical axis.

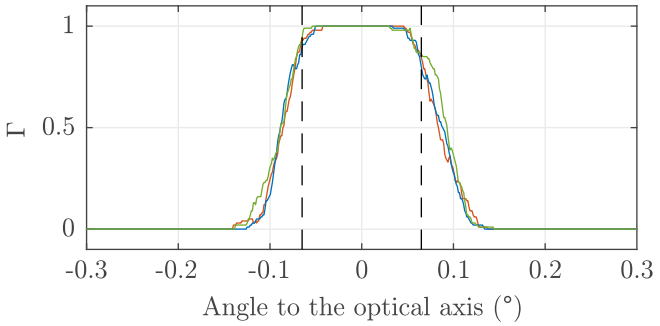

Fig. 14. Γ functions of the θ_{n-1}, θ_n, and θ_{n+1} rays as a function of the angular distance from the ray optical axis obtained at $r = 2.5$ m distance. The dashed lines represent the angular sectors of width $\pm\Delta\theta/2$ centered on the ray optical axis.

in (7) and (8) defines the maximum uncertainty allowed in the radial coordinate estimation. Note that, as introduced in Section II and described in more detail by Cattini et al. [6], even when the object is correctly detected, the value of r is not a deterministic quantity but a discrete random variable that can assume the value of the radii of several adjacent axial bins. Therefore, the probability obtained by setting $n_b = 0$ is not the simple estimate of the probability that the object is detected but the estimate of the probability that it is detected at the "exact" axial distance. Thus, when interested in the detection probability, it may be convenient to set a value of n_b greater than 0. The upper limit is given by the maximum axial error accepted by the detection, classification, or tracking algorithms used to analyze the PC. In this regard, given that, as introduced above, the axial error is partly responsible for blurring in the Cartesian representation of the edges of sharp objects, in the presence of significant axial errors, it could be more effective to analyze the PCs in spherical coordinates.

The example results shown in Section V have been obtained setting $n_b = 3$—$\Delta r \approx 6$ cm [6]. Based on the results reported by Cattini et al. [6], $n_b = 3$ reasonably allows removing the contribution due to the axial error from the estimate of the detection probability.

VII. Conclusion

Currently, the main applications of 3-D LiDARs are object perception and scene segmentation. The success of such operations depends on the processing of the LiDAR output but also inexorably depends on the quality of the PC. This study proposes a simple experimental method for estimating the "quality" of the PC in terms of errors and deformations. The starting point of the proposed analysis is the determination of the ray detection probability—the probability that the ray will report a point in the PC. As described in more detail in Section III, such a probability depends on various factors, including the power and the divergence of the emitted beam/s, the emission and collection optics, the efficiency of the receiver, and the algorithms implemented by the LiDAR for the detection of echoes. Most of this information is not provided by LiDARs manufacturers; thus, mathematical modeling is essentially impossible.

On the contrary, being the proposed method an experimental method, it does not require assumptions or simplifications

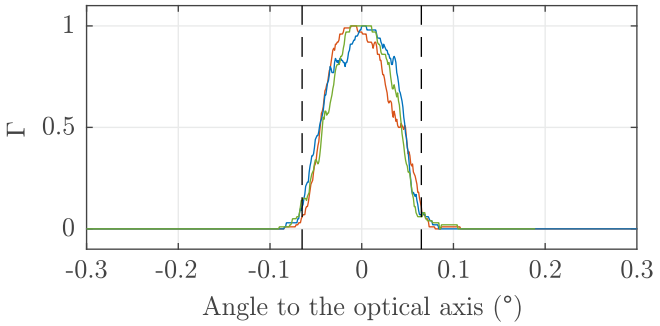

Fig. 15. Γ functions of the θ_{n-1}, θ_n, and θ_{n+1} rays as a function of the angular distance from the ray optical axis obtained at $r = 3$ m distance. The dashed lines represent the angular sectors of width $\pm\Delta\theta/2$ centered on the ray optical axis.

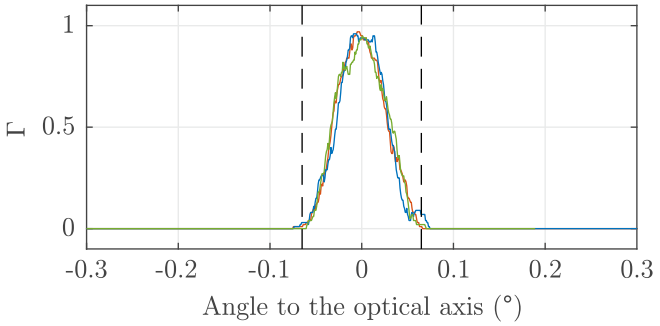

Fig. 16. Γ functions of the θ_{n-1}, θ_n, and θ_{n+1} rays as a function of the angular distance from the ray optical axis obtained at $r = 3.5$ m distance. The dashed lines represent the angular sectors of width $\pm\Delta\theta/2$ centered on the ray optical axis.

regarding the physics of the device and, therefore, regarding aspects, such as the divergence of the beams and the aberrations of the optics. Thus, the proposed method can be exploited for analyzing any LiDAR, regardless of its construction technology.

From the knowledge of the ray detection probability, all the other probabilities of interest are estimated supposing the rays have the same statistical properties and are statistically independent—independent and identically distributed random variables. Such a hypothesis can be easily verified experimentally.

The reported results were obtained by carrying out the analysis in optimal conditions, i.e., for example, with a low level

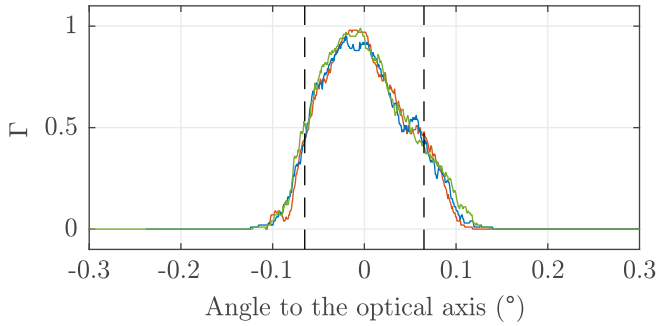

Fig. 17. Γ functions of the θ_{n-1}, θ_n, and θ_{n+1} rays as a function of the angular distance from the ray optical axis obtained at $r = 4$ m distance. The dashed lines represent the angular sectors of width $\pm\Delta\theta/2$ centered on the ray optical axis.

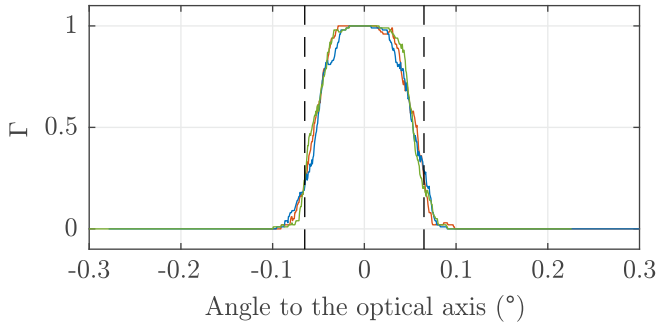

Fig. 18. Γ functions of the θ_{n-1}, θ_n, and θ_{n+1} rays as a function of the angular distance from the ray optical axis obtained at $r = 4.5$ m distance. The dashed lines represent the angular sectors of width $\pm\Delta\theta/2$ centered on the ray optical axis.

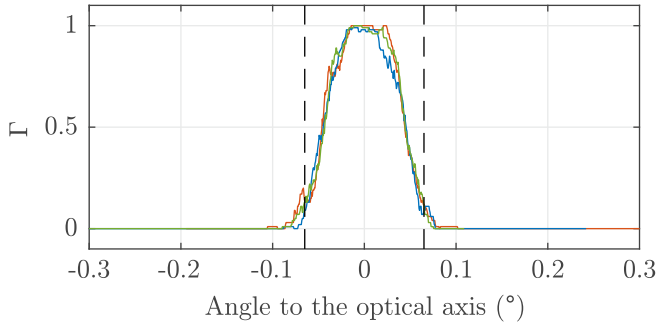

Fig. 19. Γ functions of the θ_{n-1}, θ_n, and θ_{n+1} rays as a function of the angular distance from the ray optical axis obtained at $r = 5$ m distance. The dashed lines represent the angular sectors of width $\pm\Delta\theta/2$ centered on the ray optical axis.

of background radiation noise and substantially in the absence of multiple echos. Therefore, they reasonably represent an estimate of the best obtainable detection probabilities. If interested in the performances obtainable in specific conditions of background radiation noise or multiple echos, it would be possible to investigate the specific detection probability that would be obtained in such conditions by acting on the ambient lighting and the distance d_{off} described in Fig. 5.

The possibility that the proposed method offers to estimate the ray detection probability and all the other probabilities and errors deriving from it is of significant interest in multiple applications. In particular, the proposed method can be useful to determine if a specific LiDAR can detect the objects of interest with adequate probability, thus allowing the benchmarking between different LiDAR systems.

Furthermore, by providing an estimate of the deformations and errors that will statistically affect the PC, it also allows the comparison and development of different PC processing algorithms. Indeed, as previously described, the success of subsequent operations, such as detection, classification, and tracking, depends inexorably on the specific algorithms exploited for the PC data processing. Thus, by providing an estimate of the errors and their probability of occurrence, the proposed method also allows the development or selection of the most suitable processing algorithms to operate in the presence of such errors.

In addition, it can also allow the optimization of LiDAR positioning. Indeed, if, for example, it turns out that some rays have a better $\bar{\Gamma}$ function, it would be possible to orient the LiDAR in such a way as to maximize the probability that these rays will intercept the objects of interest.

APPENDIX
Γ FUNCTIONS RECORDED AT VARIOUS DISTANCES

Figs. 13–19 show the Γ functions obtained from θ_{n-1}, θ_n, and θ_{n+1} rays as the knife distance r and the angular distance from the optical axis of the ray vary. As expected from Fig. 11, the Γ functions related to the three rays are similar to each other supporting the hypothesis that, at least in the case of adjacent beams, the ray detection probabilities are independent and identically distributed random variables.

REFERENCES

[1] H. González-Jorge, B. Riveiro, J. Armesto, and P. Arias, "Standard artifact for the geometric verification of terrestrial laser scanning systems," *Opt. Laser Technol.*, vol. 43, no. 7, pp. 1249–1256, Oct. 2011. [Online]. Available: https://www.sciencedirect.com/science/article/pii/S0030399211000697

[2] S. Cattini, L. D. Cecilia, L. Ferrari, and L. Rovati, "Optical characterization of the beams generated by 3-D LiDARs: Proposed procedure and preliminary results on MRS1000," *IEEE Trans. Instrum. Meas.*, vol. 69, no. 10, pp. 7796–7804, Oct. 2020, doi: 10.1109/TIM.2020.2984137.

[3] M. Rodríguez-Cortina, P. Adamiec, J. Barbero, X. Quintana, and M. A. Geday, "Emulation technique of multiple overlapped return echoes of a spatial LiDAR with 100-dB dynamic resolution," *IEEE Trans. Instrum. Meas.*, vol. 70, pp. 1–7, 2021.

[4] R. G. Brazeal, B. E. Wilkinson, and H. H. Hochmair, "A rigorous observation model for the Risley prism-based Livox Mid-40 LiDAR sensor," *Sensors*, vol. 21, no. 14, p. 4722, Jul. 2021. [Online]. Available: https://www.mdpi.com/1424-8220/21/14/4722

[5] S. Cattini, D. Cassanelli, L. D. Cecilia, L. Ferrari, and L. Rovati, "A procedure for the characterization and comparison of 3-D LiDAR systems," *IEEE Trans. Instrum. Meas.*, vol. 70, pp. 1–10, 2021.

[6] S. Cattini, D. Cassanelli, G. D. Loro, L. D. Cecilia, L. Ferrari, and L. Rovati, "Analysis, quantification, and discussion of the approximations introduced by pulsed 3-D LiDARs," *IEEE Trans. Instrum. Meas.*, vol. 70, pp. 1–11, 2021.

[7] W. Luo and W. Wei, "A low-cost high-resolution LiDAR system with nonrepetitive scanning," *IEEE Trans. Instrum. Meas.*, vol. 71, pp. 1–10, 2022.

[8] X. Liu, C. Yuan, and F. Zhang, "Targetless extrinsic calibration of multiple small FoV LiDARs and cameras using adaptive voxelization," *IEEE Trans. Instrum. Meas.*, vol. 71, pp. 1–12, 2022.

[9] J. Lin, S. Li, W. Dong, T. Matsumaru, and S. Xie, "Long-arm three-dimensional LiDAR for antiocclusion and antisparsity point clouds," *IEEE Trans. Instrum. Meas.*, vol. 70, pp. 1–10, 2021.

[10] A. O. Korkan and H. Yuksel, "A novel time-to-amplitude converter and a low-cost wide dynamic range FPGA TDC for LiDAR application," *IEEE Trans. Instrum. Meas.*, vol. 71, pp. 1–15, 2022.

[11] Z. Wang, X. Li, T. Bi, D. Li, and L. Xu, "A compact in situ ranging LiDAR and performance evaluation," *IEEE Trans. Instrum. Meas.*, vol. 72, pp. 1–10, 2023.
[12] D. Hanto et al., "Time of flight LiDAR employing dual-modulation frequencies switching for optimizing unambiguous range extension and high resolution," *IEEE Trans. Instrum. Meas.*, vol. 72, pp. 1–8, 2023.
[13] Z. Jeffries, J. P. Bos, P. Mcmanamon, C. Kershner, and A. Kurup, "Toward open benchmark tests for automotive LiDARs, year 1: Static range error, accuracy, and precision," *Opt. Eng.*, vol. 62, no. 3, Jan. 2023, Art. no. 031211, doi: 10.1117/1.OE.62.3.031211.
[14] S. Donati, *Electro-Optical Instrumentation: Sensing and Measuring With Lasers*. Upper Saddle River, NJ, USA: Prentice-Hall, 2004.
[15] R. Roriz, J. Cabral, and T. Gomes, "Automotive LiDAR technology: A survey," *IEEE Trans. Intell. Transp. Syst.*, vol. 23, no. 7, pp. 6282–6297, Jul. 2022.
[16] R. D. Richmond and S. C. Cain, *Direct-Detection LADAR Systems*, vol. TT85. Bellingham, WA, USA: SPIE, 2010, doi:10.1117/3.836466.
[17] P. Mc Manamon, *LiDAR Technologies and Systems*, vol. 300. Bellingham, WA, USA: SPIE, 2019, doi: 10.1117/3.2518254.
[18] W. R. McCluney, *Introduction to Radiometry and Photometry*. Norwood, MA, USA: Artech House, 1994.
[19] D. Cassanelli, S. Cattini, G. D. Loro, L. D. Cecilia, L. Ferrari, and L. Rovati, "LiDARs detected signal and target distance estimation: Measurement errors from target reflectance and multiple echos," in *Proc. IEEE Int. Workshop Metrology Automot. (MetroAutomotive)*, Jul. 2022, pp. 59–64.

Stefano Cattini (Member, IEEE) received the Ph.D. degree in electronics and telecommunications from the University of Modena and Reggio Emilia, Modena, Italy, in 2009.

From 2014 to 2019, he was the Head of research with the MS2 Laboratory, Science and Technology Park for Medicine (TPM) "Mario Veronesi," Mirandola, Italy. Since 2009, he has been with the Department of Engineering "Enzo Ferrari," University of Modena and Reggio Emilia, where he is currently an Associate Professor of electronic instrumentation and measurement science. His research interests include the design, characterization, and validation of new measurement methods and measuring systems with a particular focus on automotive and biomedical applications.

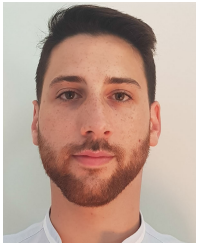

Davide Cassanelli (Graduate Student Member, IEEE) received the M.S. degree (cum laude) in electronic engineering from the University of Modena and Reggio Emilia, Modena, Italy, in 2019, and the Ph.D. degree in automotive for an intelligent mobility from the University of Bologna, Bologna, Italy, in 2023.

He works as a Research Fellow with the University of Modena and Reggio Emilia. His research interests include optoelectronic instrumentation and measuring systems, with a special focus on biomedical and automotive applications.

Luca Ferrari received the B.S., M.S., and Ph.D. degrees from the University of Modena and Reggio Emilia, Modena, Italy, in 2007, 2009, and 2013, respectively, all in electronics engineering.

He is currently the Manager of the Sensors Innovation Group, CNH Industrial Italia SpA, Modena. His research interests include optoelectronic instrumentation and measuring systems, with a special focus on biomedical and agri-food applications.

Luigi Rovati (Member, IEEE) is currently a Full Professor of electronic instrumentation and measurement science with the Department of Engineering "Enzo Ferrari," University of Modena and Reggio Emilia, Modena, Italy. He is also the Scientific Director of the MS2 Laboratory, Science and Technology Park for Medicine (TPM) "Mario Veronesi," Mirandola, Italy. The published articles production (more than 200 publications) testifies the level of the developed activity. He is also involved in various research projects between university and industrial partners. His research interests include the study and development of high-performance and innovative instrumentation.

Open Access funding provided by 'Università degli Studi di Modena e Reggio Emilia' within the CRUI CARE Agreement